Analytical Kinematic Model and RCM Control of a Parallel-Serial Steady-Hand Eye Robot

Botao Zhao[1], Mojtaba Esfandiari[1]*, Teng Long[1], Yub Heo[1],
Peter Gehlbach[2], Peter Kazanzides[1], and Iulian Iordachita[1],
1- Laboratory for Computational Sensing and Robotics,
Johns Hopkins University, Baltimore, MD, 21218, USA,
(E-mail: bzhao17, mesfand2, tlong29, yheo1, amunawa2, pkaz, iordachita@jhu.edu)
2- Wilmer Eye Institute, Johns Hopkins School of Medicine, Baltimore, MD, 21287, USA,
(E-mail: pgelbach@jhmi.edu)

Maintaining a precise remote center of motion (RCM) is essential for safe and accurate tool manipulation in retinal microsurgery. However, existing numerical Jacobian identification methods for parallel manipulators often exhibit nonlinear, workspace-dependent inaccuracies and require frequent recalibration, limiting their reliability and clinical applicability. To address these challenges, this study presents an analytical kinematic framework for a hybrid parallel–serial robot designed for retinal surgery, known as SHER 3.0. Closed-form solutions for forward and inverse kinematics, as well as analytical formulations of the direct and inverse Jacobians, are derived to ensure consistent motion estimation across the workspace. The kinematic performance of SHER 3.0 is analyzed to evaluate the manipulability and workspace efficiency. Building on these models, a model predictive control (MPC) strategy is implemented on SHER 3.0, which maintains the RCM constraint at the sclerotomy with sub-millimeter accuracy, with root mean square error (RMSE) of 0.55 ± 0.12 mm, in a pilot study on a teleportation experiment. Experimental results demonstrate the effectiveness of the proposed analytical models and control framework in enhancing motion stability and robustness and RCM control accuracy, enabling safe robot-assisted retinal microsurgery.

1 INTRODUCTION

Parallel manipulators (PMs) have attracted significant attention from both researchers and industry because of their distinct advantages over serial robot manipulators [1]. Given that their end-effector is supported by multiple kinematic chains, these systems exhibit superior structural rigidity and dynamic performance while maintaining a lower overall inertia [2]. PMs offer additional benefits such as simplified design and reduced manufacturing costs, while providing high precision and payload, even at high velocities [3]. They have found applications across a variety of fields, including pick-and-place operations [4], robotic legged landers [5], manufacturing [6], and machine tools [7], and medical robotics for surgical [8] and rehabilitation purposes [9].

Focusing on medical robotics for ophthalmic surgeries, several parallel [10] or serial [11] robotic manipulators have been developed that enable manipulation of a surgical instrument inside the eye, provide micromillimeter scale positioning accuracy, and remove hand tremor while satisfying a remote center of motion (RCM) constraint at the sclerotomy to avoid damaging the eye [12].

The Steady-Hand Eye Robots (SHERs) [13] are five-degree-of-freedom (5-DOF) manipulators, which have versions with serial and parallel mechanisms [14], developed at Johns Hopkins University for retinal microsurgery applications. Previous versions of SHER, namely SHER 2.0 and SHER 2.1, are serial manipulators with a translation accuracy of $5 \pm 2\,\mu$m [15]. The latest version of this robot, SHER 3.0, is a hybrid robot comprising a parallel Delta platform with a serial roll–tilt mechanism. [16]

Precise position control of SHER 3.0 requires accurate information on robot kinematics and Jacobian; however, modeling and calibration of parallel mechanisms are

---

*Corresponding author: Mojtaba Esfandiari
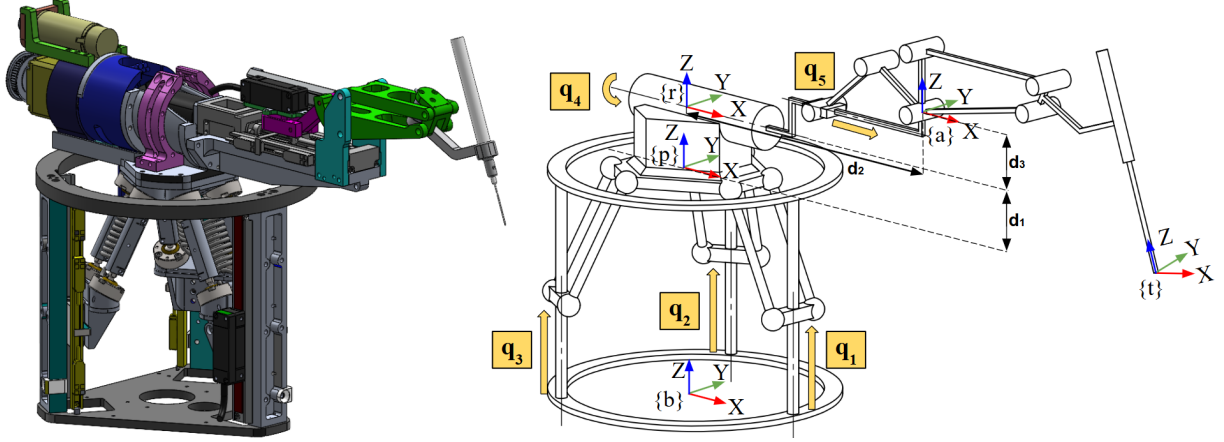(E-mail: mesfand2@jhu.edu)

Fig. 1: The CAD model (left) and schematic diagram of the SHER 3.0 kinematic (right).

challenging tasks [17]. In a previous study, the Jacobian of SHER 3.0 was calibrated using the Bernstein polynomial, resulting in a root mean square error of 20 μm [18], which satisfies the clinical precision required (about 25-30 μm) to perform microsurgical operations such as subretinal injection [12].

Since the kinematic behavior of parallel mechanisms is highly nonlinear and significantly changes over the workspace [2], one limitation of the numerical Jacobian identification methods, such as the one in [18] is that their accuracy may not remain consistent across the entire robot workspace, resulting in inconsistent and unsafe motion control. Another limitation is that their accuracy might decrease over time due to robot use; recalibration and validation are challenging and time-consuming. To resolve these limitations and gaps in science, in this study, we developed analytical models for forward and inverse kinematics and the Jacobian of the parallel robot for retinal microsurgery, the SHER 3.0, and designed a MPC-based on these models that accurately satisfies a remote center of motion RCM constraint at the eye sclerotomy.

The contributions of this work are listed as follows:

1- We developed analytical relations for the forward and inverse kinematics as well as forward and inverse Jacobians, for a parallel-serial robot manipulator, SHER 3.0, for retinal microsurgery applications.

2- We evaluated the kinematics performance of the SHER 3.0, using several kinematic-related metrics such as reachable and dexterous workspace analysis and manipulability index.

3- We implemented a MPC algorithm, using the proposed analytical kinematics and Jacobian models to enforce a RCM constraint that satisfies the clinical precision needed for retinal microsurgeries.

The remaining sections of this paper are as follows. Section 2 explains the methodologies in robot kinematics and control. Section 3 presents the experimental setup and procedure. Experimental results are presented in Section 4 and discussed in Section 5. Section 6 concludes the paper.

2 MATERIALS AND METHODS
2.1 Forward Kinematics
The proposed eye surgical robot can be decomposed into two serially connected subsystems: a parallel delta mechanism and a roll–tilt four-bar mechanism mounted on the moving platform. This decomposition allows the forward kinematics to be derived for each subsystem separately, and the complete forward kinematics of the robot is then obtained by combining the two.

2.1.1 Delta Platform
The derivation of the kinematics for the delta platform follows the approach described in [18] and [19]. As shown in Figure 2b, the base and platform joint circle radii are denoted by r_b and r_p. The angles between the i-th prismatic joint and the x-axis of the base frame are given by $\theta_{b_i} \in \left\{0, \frac{2\pi}{3}, \frac{4\pi}{3}\right\}$, while the angles between the i-th upper universal joint and the x-axis of the moving frame are $\theta_{p_i} \in \left\{0, \frac{2\pi}{3}, \frac{4\pi}{3}\right\}$. The link length between universal joints is l, with the corresponding link vector $\mathbf{l}_i = [x_{l_i}, y_{l_i}, z_{l_i}]^T$, and the prismatic joint vector $\mathbf{L}_i = [0, 0, q_i]^T$. The moving platform position vector is denoted by $\mathbf{r} = [r_x, r_y, r_z]^T$. With the above parameters, the i-th vector loop equation is:

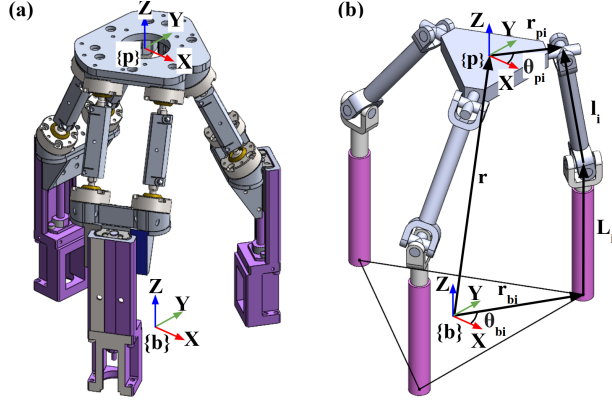$$\mathbf{l}_i = -\mathbf{L}_i - \mathbf{r}_{bi} + \mathbf{r} + \mathbf{r}_{pi} \tag{1}$$

Fig. 2: Delta platform: (a) 3D view of the mechanical structure; (b) simplified kinematic model

where

$$\mathbf{r}_{bi} = [r_b \cos \theta_{bi}, \ r_b \sin \theta_{bi}, \ 0]^T$$
$$\mathbf{r}_{pi} = [r_p \cos \theta_{pi}, \ r_p \sin \theta_{pi}, \ 0]^T$$

let $\mathbf{e}_i = \mathbf{L}_i + \mathbf{r}_{bi} - \mathbf{r}_{pi}$ and rewrite Eq.(1) as

$$\mathbf{l}_i = \mathbf{r} - \mathbf{e}_i \qquad (2)$$

Taking the dot product of Eq.(2) with itself on both sides:

$$\mathbf{l}_i^T \mathbf{l}_i = (\mathbf{r} - \mathbf{e}_i)^T (\mathbf{r} - \mathbf{e}_i) \qquad (3)$$

which can be expanded into the scalar form:

$$l^2 = \mathbf{r}^T \mathbf{r} - 2\mathbf{r}^T \mathbf{e}_i + \mathbf{e}_i^T \mathbf{e}_i \qquad (4)$$

From Eq.(4), three scalar equations can be written for $i = 1, 2, 3$ as

$$\begin{aligned}
l^2 &= \mathbf{r}^T \mathbf{r} - 2\mathbf{r}^T \mathbf{e}_1 + \mathbf{e}_1^T \mathbf{e}_1 \\
l^2 &= \mathbf{r}^T \mathbf{r} - 2\mathbf{r}^T \mathbf{e}_2 + \mathbf{e}_2^T \mathbf{e}_2 \\
l^2 &= \mathbf{r}^T \mathbf{r} - 2\mathbf{r}^T \mathbf{e}_3 + \mathbf{e}_3^T \mathbf{e}_3
\end{aligned} \qquad (5)$$

Pairwise subtraction of these equations, and combine like terms:

$$\begin{aligned}
0 &= -2\mathbf{r}^T(\mathbf{e}_2 - \mathbf{e}_1) + \left(\mathbf{e}_2^T \mathbf{e}_2 - \mathbf{e}_1^T \mathbf{e}_1\right) \\
0 &= -2\mathbf{r}^T(\mathbf{e}_3 - \mathbf{e}_1) + \left(\mathbf{e}_3^T \mathbf{e}_3 - \mathbf{e}_1^T \mathbf{e}_1\right)
\end{aligned} \qquad (6)$$

Let $h_1 = \dfrac{\mathbf{e}_2^T \mathbf{e}_2 - \mathbf{e}_1^T \mathbf{e}_1}{2}, \quad h_2 = \dfrac{\mathbf{e}_3^T \mathbf{e}_3 - \mathbf{e}_1^T \mathbf{e}_1}{2}$

Eq.(6) can be written as:

$$\begin{aligned}
\mathbf{r}^T(\mathbf{e}_2 - \mathbf{e}_1) - h_1 &= 0 \\
\mathbf{r}^T(\mathbf{e}_3 - \mathbf{e}_1) - h_2 &= 0
\end{aligned} \qquad (7)$$

Since all of the elements in $(\mathbf{e}_2 - \mathbf{e}_1)$ and $(\mathbf{e}_3 - \mathbf{e}_1)$ are constants, let

$$\mathbf{e}_2 - \mathbf{e}_1 = [x_{21}, y_{21}, z_{21}]^T$$
$$\mathbf{e}_3 - \mathbf{e}_1 = [x_{31}, y_{31}, z_{31}]^T$$

Then Eq.(7) can be expressed as:

$$\begin{aligned}
x_{21}r_x + y_{21}r_y + z_{21}r_z - h_1 &= 0 \\
x_{31}r_x + y_{31}r_y + z_{31}r_z - h_2 &= 0
\end{aligned} \qquad (8)$$

Rearranging Eq.(8):

$$\begin{aligned}
r_x &= \frac{(y_{31}z_{21}/y_{21} - z_{31})}{(x_{31} - y_{31}x_{21}/y_{21})}r_z + \frac{(h_2 - y_{31}h_1/y_{21})}{(x_{31} - y_{31}x_{21}/y_{21})} \\
r_y &= \frac{(x_{31}z_{21}/x_{21} - z_{31})}{(y_{31} - x_{31}y_{21}/x_{21})}r_z + \frac{(h_2 - x_{31}h_1/x_{21})}{(y_{31} - x_{31}y_{21}/x_{21})}
\end{aligned} \qquad (9)$$

Let

$$k_1 = \frac{(y_{31}z_{21}/y_{21} - z_{31})}{(x_{31} - y_{31}x_{21}/y_{21})}, \ k_2 = \frac{(h_2 - y_{31}h_1/y_{21})}{(x_{31} - y_{31}x_{21}/y_{21})}$$
$$k_3 = \frac{(x_{31}z_{21}/x_{21} - z_{31})}{(y_{31} - x_{31}y_{21}/x_{21})}, \ k_4 = \frac{(h_2 - x_{31}h_1/x_{21})}{(y_{31} - x_{31}y_{21}/x_{21})}$$

Then substituting Eq.(9) into the first row of Eq.(5), where $\mathbf{e}_1 = [e_{1x}, e_{1y}, e_{1z}]^T$:

$$\begin{aligned}
l^2 &= \begin{bmatrix} k_1 r_z + k_2, & k_3 r_z + k_4, & r_z \end{bmatrix} \begin{bmatrix} k_1 z + k_2 \\ k_3 z + k_4 \\ r_z \end{bmatrix} \\
&\quad - 2\begin{bmatrix} k_1 r_z + k_2, & k_3 r_z + k_4, & r_z \end{bmatrix} \begin{bmatrix} e_{1x} \\ e_{1y} \\ e_{1z} \end{bmatrix} + \mathbf{e}_1^T \mathbf{e}_1
\end{aligned} \qquad (10)$$

Let

$$T_1 = k_1^2 + k_3^2 + 1$$
$$T_2 = k_1 k_2 + k_3 k_4 - e_{1x}k_1 - e_{1y}k_3 - e_{1z}$$
$$T_3 = k_2^2 + k_4^2 - 2e_{1x}k_2 - 2e_{1y}k_4 - l^2 + e_{1x}^2 + e_{1y}^2 + e_{1z}^2$$

Rearranging Eq.(10):

$$r_z = \frac{-T_2 \pm \sqrt{T_2^2 - T_1 T_3}}{T_1} \quad (11)$$

Since the moving platform must be above the base plane, only positive r_z solution is valid.

Thus, Eq.(9) and Eq.(11) form the forward kinematic solution $\mathbf{r} = [r_x, \ r_y, \ r_z]^T$ of the delta platform. The homogeneous transformation matrix from base frame $\{b\}$ to platform frame $\{p\}$ is:

$$T_{bp} = \begin{bmatrix} \mathbf{I}_{3\times 3} & \mathbf{r}_{3\times 1} \\ \mathbf{0}_{1\times 3} & 1 \end{bmatrix} \quad (12)$$

2.1.2 Rotation Four-bar Mechanism

As shown in Fig.3, the control inputs of this rotation four-bar mechanism are the roll angle ψ and the linear actuator stroke length s. Due to the nature of the four-bar linkage, the motion of the tool involves both rotation and translation. However, these two motions are kinematically coupled, knowing one uniquely determines the other. The present derivation extends the approach introduced in [20].

Link AB is relatively fixed on the roll mechanism, and point P maintains fixed relative to link CD. For simplicity, point A is defined as the origin of the coordinate system. As the stroke length s is known:

$$x_{AR} = x_{AR_{max}} - s \quad (13)$$

where $x_{AR_{max}}$ is the max horizontal distance between the origin to the slider, which is known based on the design parameter, and z_{AR} is also a fixed value, representing the height from the linear guide rail to the frame $\{a\}$.

Thus,

$$L_{AR} = \sqrt{x_{AR}^2 + z_{AR}^2} \quad (14)$$

$$\alpha_4 = \arctan(y_{AR}, z_{AR}) \quad (15)$$

As the lengths of AQ and QR are known, from the law of cosine:

$$\alpha_3 = \arccos\left(\frac{L_{AR}^2 + L_{AQ}^2 - L_{QR}^2}{2 L_{AR} L_{AQ}}\right) \quad (16)$$

Since ϕ_1 and ϕ_2 are angles with fixed values, and α_3, α_4 are known:

$$\theta_1 = 180° - (\phi_2 + \alpha_3 + \alpha_4) \quad (17)$$

$$\alpha_1 = \phi_1 - \theta_1 \quad (18)$$

Form the law of cosine again:

$$L_{BD} = \sqrt{L_{AB}^2 + L_{DA}^2 - 2 L_{AB} L_{DA} \cos(\alpha_1)} \quad (19)$$

$$\beta_1 = \arccos\left(\frac{L_{AB}^2 + L_{BD}^2 - L_{DA}^2}{2 L_{AB} L_{BD}}\right) \quad (20)$$

$$\delta = \arccos\left(\frac{L_{BD}^2 + L_{CD}^2 - L_{BC}^2}{2 L_{BD} L_{CD}}\right) \quad (21)$$

$$\begin{aligned} \theta_2 &= 180° - ((180° - \beta_1 - \phi_1) + \delta) \\ &= \beta_1 + \phi_1 - \delta \end{aligned} \quad (22)$$

Since ϕ_3 and ϕ_4 are also known and the lengths of AD and DP are constants, the x and y coordinates of point $\mathbf{P}$ in frame $\{a\}$ can be directly computed:

$$\begin{aligned} P_x &= \cos(\theta_1) L_{DA} + \cos(\theta_2 - \phi_3) L_{DP} \\ P_z &= \sin(\theta_1) L_{DA} + \sin(\theta_2 - \phi_3) L_{DP} \end{aligned} \quad (23)$$

Let $\theta = 90° - \phi_4 - (\phi_3 - \theta_2)$, the angle between the x-axis of frame $\{a\}$ and the x-axis of frame $\{t\}$. Then the transformation matrix can be expressed as:

$$T_{at} = \begin{bmatrix} \cos(\theta) & 0 & \sin(\theta) & P_x \\ 0 & 1 & 0 & 0 \\ -\sin(\theta) & 0 & \cos(\theta) & P_z \\ 0 & 0 & 0 & 1 \end{bmatrix} \quad (24)$$

Thus, given the stroke length s, we can then determine the tool frame's position and orientation relative to frame $\{a\}$. With the transformations T_{bp} and T_{at} established, the remaining step to express the tool-tip position
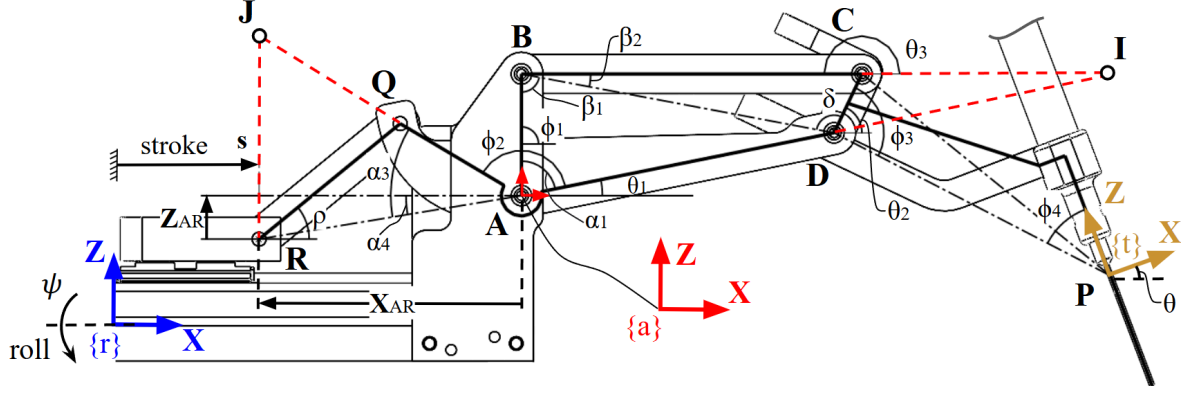
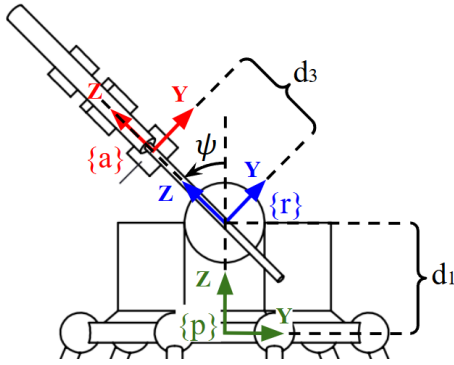Fig. 3: Side view of the roll–tilt mechanism showing the reference frames and geometric parameters.

Fig. 4: Simplified front view of the roll-tilt mechanism

and orientation in the base frame $\{b\}$ is to determine the transformation T_{pa}.

As illustrated in Fig. 4, the roll angle ψ is defined with respect to the z-axis of frame $\{p\}$. The roll axis is located a distance d_1 above the delta platform frame $\{p\}$, while frame $\{a\}$ is positioned a distance d_3 along the z-axis of frame $\{r\}$. In addition, the displacement between frames $\{r\}$ and $\{a\}$ along the x-axis is d_2, as shown in Fig. 1.

Accordingly, the transformation matrices T_{pr} and T_{ra} can be written as:

$$
T_{pr} = \begin{bmatrix} 1 & 0 & 0 & 0 \\ 0 & \cos(\psi) & -\sin(\psi) & 0 \\ 0 & \sin(\psi) & \cos(\psi) & d_1 \\ 0 & 0 & 0 & 1 \end{bmatrix}
$$

$$
T_{ra} = \begin{bmatrix} 1 & 0 & 0 & d_2 \\ 0 & 1 & 0 & 0 \\ 0 & 0 & 1 & d_3 \\ 0 & 0 & 0 & 1 \end{bmatrix}
$$
(25)

Then, by multiplying the two matrices, we obtain the transformation matrix T_{pa}:

$$
\begin{aligned}
T_{pa} &= T_{pr} T_{ra} \\
&= \begin{bmatrix} 1 & 0 & 0 & d_2 \\ 0 & \cos(\psi) & -\sin(\psi) & -\sin(\psi)d_3 \\ 0 & \sin(\psi) & \cos(\psi) & \cos(\psi)d_3 + d_1 \\ 0 & 0 & 0 & 1 \end{bmatrix}
\end{aligned}
$$
(26)

Thus, the transformation from base frame $\{b\}$ to tool frame $\{t\}$ is:

$$
\begin{aligned}
T_{bt} &= T_{bp} T_{pa} T_{at} \\
&= \begin{bmatrix} \cos(\theta) & 0 & \sin(\theta) & x_{bt} \\ \sin(\theta)\sin(\psi) & \cos(\psi) & -\cos(\theta)\sin(\psi) & y_{bt} \\ -\sin(\theta)\cos(\psi) & \sin(\psi) & \cos(\theta)\cos(\psi) & z_{bt} \\ 0 & 0 & 0 & 1 \end{bmatrix}
\end{aligned}
$$
(27)

where

$$
\begin{aligned}
x_{bt} &= P_x + d_2 + r_x \\
y_{bt} &= -\sin(\psi)P_z - \sin(\psi)d_3 + r_y \\
z_{bt} &= \cos(\psi)P_z + \cos(\psi)d_3 + d_1 + r_z
\end{aligned}
$$

2.2 Inverse Kinematics

Similar to the forward kinematics derivation, the inverse kinematics of each subsystem is derived independently. The results are then combined to form the complete inverse kinematics of the robot.

2.2.1 Delta Platform

Write Eq.(1) in matrix form:

$$\begin{bmatrix} l_{ix} \\ l_{iy} \\ l_{iz} \end{bmatrix} = -\begin{bmatrix} 0 \\ 0 \\ q_i \end{bmatrix} - \begin{bmatrix} r_b\cos(\theta_{bi}) \\ r_b\sin(\theta_{bi}) \\ 0 \end{bmatrix} + \begin{bmatrix} r_x \\ r_y \\ r_z \end{bmatrix} + \begin{bmatrix} r_p\cos(\theta_{pi}) \\ r_p\sin(\theta_{pi}) \\ 0 \end{bmatrix} \quad (28)$$

Since the length of each link is $l = \sqrt{l_{ix}^2 + l_{iy}^2 + l_{iz}^2}$, Eq.(28) can be written as:

$$\begin{aligned} l^2 &= l_{ix}^2 + l_{iy}^2 + l_{iz}^2 \\ &= (r_x + a_i)^2 + (r_y + b_i)^2 + (r_z - q_i)^2 \end{aligned} \quad (29)$$

where

$$\begin{aligned} a_i &= -r_b\cos\theta_{bi} + r_p\cos\theta_{pi} \\ b_i &= -r_b\sin\theta_{bi} + r_p\sin\theta_{pi} \end{aligned}$$

Reorganizing Eq.(29):

$$q_i = r_z - \sqrt{l^2 - (r_x + a_i)^2 - (r_y + b_i)^2} \quad (30)$$

This gives the prismatic actuator extension for each leg, where $i = 1, 2, 3$.

2.2.2 Rotation Four-bar Mechanism

The inverse kinematics of the four-bar mechanism presents more complexity. Given the tool tilt angle θ, the angle between link CD and the horizontal axis can be easily obtained as $\theta_2 = \theta + \phi_3 + \phi_4 - 90°$. However, substituting θ_2 back into Eq.(22) to solve for θ_1 and stroke length s introduces difficulties, as both β_1 and δ remain unknown since the length of BD varies. Solving for these variables would require handling a set of quadratic equations, which can be computationally expensive.

A more efficient approach is to derive the inverse kinematics directly from its geometry by translating edges AB and BC to construct a new parallelogram $ABCE$, as shown in Figure 5.

It is obvious to get the following relations:

$$\begin{aligned} L_{DF} &= \cos(\theta_2)L_{CD} - \cos(\phi_1)L_{AB} \\ L_{EF} &= \sin(\phi_1)L_{AB} - \sin(\theta_2)L_{CD} \\ L_{DE} &= \sqrt{L_{DF}^2 + L_{EF}^2} \end{aligned}$$
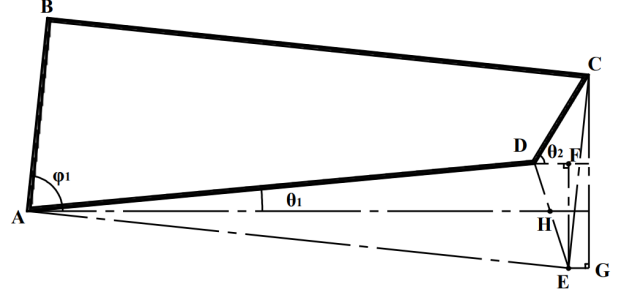

Fig. 5: Close up of the four-bar mechanism geometry

Given the lengths of AD, AE, and DE, using the law of cosine:

$$\begin{aligned} \angle ADH &= \arccos\left(\frac{L_{AD}^2 + L_{DE}^2 - L_{AE}^2}{2L_{AD}L_{DE}}\right) \\ \angle AHD &= \angle FDH = \arctan(L_{EF}, L_{DF}) \\ \theta_1 &= 180° - \angle ADH - \angle AHD \end{aligned}$$

Then, we can use θ_1 to calculate the stroke length s.

Let $\alpha = \alpha_3 + \alpha_4$:

$$\begin{aligned} \alpha &= 180° - \theta_1 - \phi_2 \\ x_{AR} &= \cos(\alpha)L_{AQ} + \sqrt{L_{QR}^2 - (\sin(\alpha)L_{AQ} - y_{AR})^2} \\ s &= x_{AR_{max}} - x_{AR} \end{aligned}$$

Since the roll angle and stroke length are directly controlled by the revolute and linear actuators, the roll and prismatic joint variables are given by $\psi = q_4$, $s = q_5$. This leads to:

$$\begin{aligned} q_4 &= \psi \\ q_5 &= x_{AR_{max}} - x_{AR}(\theta) \end{aligned} \quad (31)$$

where ψ and θ denote the prescribed orientation of the tool.

Given the tool tip position $\mathbf{P}$ expressed in frame $\{a\}$ as $\mathbf{P}_{\{a\}}$, its coordinates in the base frame $\{b\}$, denoted as $\mathbf{P}_{\{b\}}$, can be obtained from Eq.(27):

$$\mathbf{P}_{\{b\}} = \begin{bmatrix} P_{x\{b\}} \\ P_{y\{b\}} \\ P_{z\{b\}} \end{bmatrix} = \begin{bmatrix} P_{x\{a\}} + d_2 + r_x \\ -\sin(\psi)P_{z\{a\}} - \sin(\psi)d_3 + r_y \\ \cos(\psi)P_{z\{a\}} + \cos(\psi)d_3 + d_1 + r_z \end{bmatrix} \quad (32)$$

The base-to-platform vector $\mathbf{r} = [r_x, r_y, r_z]^T$ is then obtained as:

$$\begin{bmatrix} r_x \\ r_y \\ r_z \end{bmatrix} = \mathbf{P}_{\{b\}} - \begin{bmatrix} P(q_5)_{x\{a\}} + d_2 \\ -\sin(q_4)P(q_5)_{z\{a\}} - \sin(q_4)d_3 \\ \cos(q_4)P(q_5)_{z\{a\}} + \cos(q_4)d_3 + d_1 \end{bmatrix} \tag{33}$$

Then plugging Eq.(33) into Eq.(30) gives the actuator displacements q_1, q_2, q_3.

Thus, Eq.(30), (31), (33) form the inverse kinematics, proceed as follows: the inputs are the tool position $\mathbf{P}_{\{b\}}$ and orientation (ψ, θ). From ψ and θ, the joint values q_4 and q_5 are obtained, which in turn determine $P_{x\{a\}}$ and $P_{z\{a\}}$. These allow the computation of $\mathbf{r}$, and finally lead to the actuator displacements q_1, q_2, q_3.

2.3 Jacobian

To relate the joint velocities to the tool-tip velocity, the system Jacobian is required. The tool-tip velocity and the joint velocities are defined as

$$\mathbf{V} = \begin{bmatrix} \dot{x} \ \dot{y} \ \dot{z} \ \dot{\theta}_x \ \dot{\theta}_y \ \dot{\theta}_z \end{bmatrix}^T_{\{b\}}, \quad \dot{\mathbf{q}} = \begin{bmatrix} \dot{q}_1 \ \dot{q}_2 \ \dot{q}_3 \ \dot{q}_4 \ \dot{q}_5 \end{bmatrix}^T$$

Throughout this section, the term Jacobian refers to the spatial Jacobian, where all quantities are expressed in the base frame $\{b\}$. The mapping between the joint velocities and the tool-tip velocity is given by

$$\mathbf{V} = \mathbf{J}\dot{\mathbf{q}} \tag{34}$$

where $\mathbf{J} \in \mathbb{R}^{6 \times 5}$ is the Jacobian matrix. Since q_1, q_2, q_3 only generate translational motions, the upper-left 3×3 block of $\mathbf{J}$ is the Jacobian of the delta platform, denoted $\mathbf{J}_D$. To find $\mathbf{J}_D$, let $\dot{\mathbf{r}} = [\dot{r}_x, \dot{r}_y, \dot{r}_z]^T$ be the delta platform velocity, and $\dot{\mathbf{L}}_i = [0, 0, \dot{q}_i]^T$ the rate of change of each prismatic joint. Rearranging Eq.(1) and taking derivative to both side:

$$\dot{\mathbf{L}}_i = \dot{\mathbf{r}} - \dot{\mathbf{l}}_i - \dot{\mathbf{r}}_{bi} + \dot{\mathbf{r}}_{pi} \tag{35}$$

Since all of the elements in $\mathbf{r}_{bi}$ and $\mathbf{r}_{pi}$ are constants, $\dot{\mathbf{r}}_{bi} = \dot{\mathbf{r}}_{pi} = 0$. Thus,

$$\begin{aligned} \dot{\mathbf{L}}_i &= \dot{\mathbf{r}} - \dot{\mathbf{l}}_i \\ &= \dot{\mathbf{r}} - (\omega_i \times \mathbf{l}_i) \end{aligned} \tag{36}$$

Dot-multiplying $\mathbf{l}_i$ to both side:

$$\mathbf{l}_i \cdot \dot{\mathbf{L}}_i = \mathbf{l}_i \cdot \dot{\mathbf{r}} - \mathbf{l}_i \cdot (\omega_i \times \mathbf{l}_i) \tag{37}$$

Since $\mathbf{l}_i$ is perpendicular to $\omega_i \times \mathbf{l}_i$:

$$\mathbf{l}_i^T \dot{\mathbf{L}}_i = \mathbf{l}_i^T \dot{\mathbf{r}} \tag{38}$$

$$\begin{bmatrix} l_{ix} \ l_{iy} \ l_{iz} \end{bmatrix} \begin{bmatrix} 0 \\ 0 \\ \dot{q}_i \end{bmatrix} = \begin{bmatrix} l_{ix} \ l_{iy} \ l_{iz} \end{bmatrix} \begin{bmatrix} \dot{r}_x \\ \dot{r}_y \\ \dot{r}_z \end{bmatrix} \tag{39}$$

$$l_{iz}\dot{q}_i = l_{ix}\dot{r}_x + l_{iy}\dot{r}_y + l_{iz}\dot{r}_z \tag{40}$$

expand Eq.(40) with $i = 1, 2, 3$:

$$\begin{bmatrix} l_{1z} & 0 & 0 \\ 0 & l_{2z} & 0 \\ 0 & 0 & l_{3z} \end{bmatrix} \begin{bmatrix} \dot{q}_1 \\ \dot{q}_2 \\ \dot{q}_3 \end{bmatrix} = \begin{bmatrix} l_{1x} \ l_{1y} \ l_{1z} \\ l_{2x} \ l_{2y} \ l_{2z} \\ l_{3x} \ l_{3y} \ l_{3z} \end{bmatrix} \begin{bmatrix} \dot{r}_x \\ \dot{r}_y \\ \dot{r}_z \end{bmatrix} \tag{41}$$

Thus we can obtain:

$$\dot{\mathbf{r}} = \mathbf{J}_D \dot{\mathbf{q}} \tag{42}$$

where

$$\mathbf{J}_D = \begin{bmatrix} l_{1x} \ l_{1y} \ l_{1z} \\ l_{2x} \ l_{2y} \ l_{2z} \\ l_{3x} \ l_{3y} \ l_{3z} \end{bmatrix}^{-1} \begin{bmatrix} l_{1z} & 0 & 0 \\ 0 & l_{2z} & 0 \\ 0 & 0 & l_{3z} \end{bmatrix} \tag{43}$$

is the 3×3 Jacobian matrix of the delta platform.

The kinematic contributions of q_4 and q_5 require more careful consideration. As discussed previously, the four-bar linkage introduces coupled motion: actuation of q_5 generates both translation and rotation, while q_4 also contributes to the linear velocity due to the tool tip being offset from its axis of rotation.

Taking derivative to Eq.(23) gives the linear velocity of the tool tip:

$$\begin{aligned} \dot{P}_x &= -\sin(\theta_1)L_{DA}\dot{\theta}_1 - \sin(\theta_2 - \phi_3)L_{DP}\dot{\theta}_2 \\ \dot{P}_z &= \cos(\theta_1)L_{DA}\dot{\theta}_1 + \cos(\theta_2 - \phi_3)L_{DP}\dot{\theta}_2 \end{aligned} \tag{44}$$

However, the expressions for $\dot{\theta}_1$ and $\dot{\theta}_2$ involve derivatives of arctan and arccos functions, which lead to algebraically tedious forms. To overcome this, instantaneous center of velocity (ICV) method provides a more compact and intuitive formulation. The principle is that, at any given instant, a rigid body in planar motion can be treated as a pure rotation about a unique point in space, referred to as its instantaneous center. For the four-bar mechanism, these centers are denoted as points **I** and **J**, as illustrated in Figure 3a.

For example, at any instant, link **QR** can be assumed to be in pure rotation with respect to the point **J**, where **QJ** is perpendicular to the velocity of point **Q** and **RJ** is perpendicular to the velocity of point **R**.

Then, from the geometry above:

$$
\begin{aligned}
L_{JR} &= \tan(\alpha) \cdot x_{AR} - z_{AR} \\
L_{JQ} &= \sec(\alpha) \cdot x_{AR} - L_{AQ}
\end{aligned}
\tag{45}
$$

$$
\dot{\rho} = \frac{\dot{s}}{L_{JR}}, \quad L_{AQ} \cdot \dot{\alpha} = -L_{JQ} \cdot \dot{\rho}
\tag{46}
$$

$$
\dot{\theta}_1 = \dot{\alpha} = \frac{L_{JQ}}{L_{AQ} L_{JR}} \dot{s}
\tag{47}
$$

Similarly, link **CD** can be assumed to be in pure rotation with respect to the point **I**, where **CI** is perpendicular to the velocity of point **C** and **DI** is perpendicular to the velocity of point **D**.

$$
\beta_2 = \arccos\left(\frac{L_{BC}^2 + L_{BD}^2 - L_{CD}^2}{2 L_{BC} L_{BD}}\right)
\tag{48}
$$

Let $\beta = \beta_1 + \beta_2$:

$$
\angle AIB = 180° - \alpha_1 - \beta
\tag{49}
$$

Then, apply the law of sine:

$$
\frac{L_{AB}}{\sin(\angle AIB)} = \frac{L_{IA}}{\sin(\beta)} = \frac{L_{IB}}{\sin(\alpha_1)}
\tag{50}
$$

Since $\sin(180° - \alpha_1 - \beta) = \sin(\alpha_1 + \beta)$:

$$
\begin{aligned}
L_{IA} &= \frac{L_{AB} \cdot \sin(\beta)}{\sin(\alpha_1 + \beta)} \\
L_{ID} &= L_{IA} - L_{DA}
\end{aligned}
\tag{51}
$$

Using instantaneous center method:

$$
\begin{aligned}
\dot{\theta}_1 L_{DA} &= -\dot{\theta}_2 L_{ID} \\
\dot{\theta}_2 &= -\frac{L_{DA}}{L_{ID}} \dot{\theta}_1
\end{aligned}
\tag{52}
$$

From Eq.(47), since $\dot{\theta}_1 = \frac{L_{JQ}}{L_{AQ} L_{JR}} \dot{s}$:

$$
\dot{\theta}_2 = -\frac{L_{DA} L_{JQ}}{L_{ID} L_{AQ} L_{JR}} \dot{s}
\tag{53}
$$

Then, plugging Eq.(47) and Eq.(53) into Eq.(44):

$$
\begin{aligned}
\dot{P}_{x\{a\}} &= \left(-\sin(\theta_1)\frac{L_{DA} L_{JQ}}{L_{AQ} L_{JR}} + \sin(\theta_2 - \phi_3)\frac{L_{DP} L_{DA} L_{JQ}}{L_{ID} L_{AQ} L_{JR}} \right) \dot{s} \\
\dot{P}_{z\{a\}} &= \left(\cos(\theta_1)\frac{L_{DA} L_{JQ}}{L_{AQ} L_{JR}} - \cos(\theta_2 - \phi_3)\frac{L_{DP} L_{DA} L_{JQ}}{L_{ID} L_{AQ} L_{JR}} \right) \dot{s}
\end{aligned}
\tag{54}
$$

Let:

$$
\begin{aligned}
A &= \left(-\sin(\theta_1)\frac{L_{DA} L_{JQ}}{L_{AQ} L_{JR}} + \sin(\theta_2 - \phi_3)\frac{L_{DP} L_{DA} L_{JQ}}{L_{ID} L_{AQ} L_{JR}} \right) \\
B &= \left(\cos(\theta_1)\frac{L_{DA} L_{JQ}}{L_{AQ} L_{JR}} - \cos(\theta_2 - \phi_3)\frac{L_{DP} L_{DA} L_{JQ}}{L_{ID} L_{AQ} L_{JR}} \right)
\end{aligned}
$$

This gives a clear and compact expression for the velocity of point **P** as a function of $\dot{s}$:

$$
\dot{P}_{x\{a\}} = A\dot{s}, \quad \dot{P}_{z\{a\}} = B\dot{s}
$$

All velocity components above are respect to frame $\{a\}$. According to Figure 3b, the corresponding tool-tip velocity in the Delta platform frame $\{p\}$ can be readily derived as:

$$
\begin{bmatrix} \dot{x} \\ \dot{y} \\ \dot{z} \\ \dot{\theta}_x \\ \dot{\theta}_y \\ \dot{\theta}_z \end{bmatrix}_{\{p\}} = \begin{bmatrix} \dot{P}_{x\{a\}} \\ -\sin(\psi)\dot{P}_{z\{a\}} - \cos(\psi)\dot{\psi}(P_{z\{a\}} + d_3) \\ \cos(\psi)\dot{P}_{z\{a\}} - \sin(\psi)\dot{\psi}(P_{z\{a\}} + d_3) \\ \dot{\psi} \\ \cos(\psi)\dot{\theta}_2 \\ \sin(\psi)\dot{\theta}_2 \end{bmatrix}
\tag{55}
$$

Since $\dot{\psi} = \dot{q}_4$ and $\dot{s} = \dot{q}_5$, Eq.(55) can be written as:

$$\begin{bmatrix} \dot{x} \\ \dot{y} \\ \dot{z} \\ \dot{\theta}_x \\ \dot{\theta}_y \\ \dot{\theta}_z \end{bmatrix}_{\{p\}} = \underbrace{\begin{bmatrix} 0 & A \\ -\cos(q_4)(P_{z\{a\}} + d_3) & -\sin(q_4)B \\ -\sin(q_4)(P_{z\{a\}} + d_3) & \cos(q_4)B \\ 1 & 0 \\ 0 & \cos(q_4)\frac{L_{DA}L_{JQ}}{L_{ID}L_{AQ}L_{JR}} \\ 0 & \sin(q_4)\frac{L_{DA}L_{JQ}}{L_{ID}L_{AQ}L_{JR}} \end{bmatrix}}_{\mathbf{J}_{RT}} \begin{bmatrix} \dot{q}_4 \\ \dot{q}_5 \end{bmatrix}$$

(56)

Because there is no rotation between the base frame $\{b\}$ and the delta platform frame $\{p\}$, the velocity of the tool tip expressed in $\{b\}$ is simply the sum of the delta platform's velocity in $\{b\}$ and the tool tip's velocity in fixed $\{p\}$ frame. This provides all the necessary components for assembling the spatial Jacobian:

$$\mathbf{J} = \begin{bmatrix} \mathbf{J}_D & \mathbf{J}_{RT} \\ \mathbf{0}_{3\times3} & \end{bmatrix}$$

(57)

where $\mathbf{J}_D \in \mathbb{R}^{3\times3}$ is the Jacobian of the delta positioning platform, controlled by joints q_1, q_2, and q_3. $\mathbf{J}_{RT} \in \mathbb{R}^{6\times2}$ is the Jacobian of the roll-tilt mechanism, controlled by joints q_4 and q_5.

2.4 Inverse Jacobian

Similar to Eq.(34), the Jacobian Inverse is defined as:

$$\dot{\mathbf{q}} = \mathbf{J}^{-1}\mathbf{V}$$

(58)

where $\mathbf{J}^{-1} \in \mathbb{R}^{5\times6}$ is the Jacobian Inverse matrix. From Eq.(40), the desired platform velocity can be directly related to the corresponding joint velocities as:

$$\dot{q}_i = \frac{l_{ix}}{l_{iz}}\dot{r}_x + \frac{l_{iy}}{l_{iz}}\dot{r}_y + \dot{r}_z$$

(59)

Focusing on the delta platform, the joint velocities associated with a given linear platform velocity are:

$$\begin{bmatrix} \dot{q}_1 \\ \dot{q}_2 \\ \dot{q}_3 \end{bmatrix}_{delta} = \begin{bmatrix} \frac{l_{1x}}{l_{1z}} & \frac{l_{1y}}{l_{1z}} & 1 \\ \frac{l_{2x}}{l_{2z}} & \frac{l_{2y}}{l_{2z}} & 1 \\ \frac{l_{3x}}{l_{3z}} & \frac{l_{3y}}{l_{3z}} & 1 \end{bmatrix} \begin{bmatrix} \dot{r}_x \\ \dot{r}_y \\ \dot{r}_z \end{bmatrix}$$

(60)

where the coefficient matrix depends on the limb geometry $\mathbf{q}$ of the delta mechanism. Eq.(60) maps the

platform velocities to joint-space velocities for the delta stage, defining the top-left block of the inverse Jacobian.

For the roll and tilt joints, since the tool tip is not located along their axes of rotation, both roll and tilt introduce linear displacements in addition to their rotational effects. While angular velocities $\dot{\theta}_x, \dot{\theta}_y, \dot{\theta}_z$ will cause nonzero $\dot{x}, \dot{y}, \dot{z}$, these induced translations can be determined analytically, and these induced velocities ban be compensated by subtracting them from the delta platform velocities. The translational velocities induced by the roll-tilt mechanism can be expressed as:

$$\begin{bmatrix} \dot{x} \\ \dot{y} \\ \dot{z} \end{bmatrix}_{\{p\}} = \begin{bmatrix} \dot{P}_{x\{a\}} \\ -\sin(\psi)\dot{P}_{z\{a\}} - \cos(\psi)\dot{\psi}(P_{z\{a\}} + d_3) \\ \cos(\psi)\dot{P}_{z\{a\}} - \sin(\psi)\dot{\psi}(P_{z\{a\}} + d_3) \end{bmatrix}$$

(61)

By plugging Eq.(61) into Eq.(60), the joint velocities required to compensate the induced linear motion are:

$$\begin{bmatrix} \dot{q}_1 \\ \dot{q}_2 \\ \dot{q}_3 \end{bmatrix} = \begin{bmatrix} \frac{l_{1x}}{l_{1z}} & \frac{l_{1y}}{l_{1z}} & 1 \\ \frac{l_{2x}}{l_{2z}} & \frac{l_{2y}}{l_{2z}} & 1 \\ \frac{l_{3x}}{l_{3z}} & \frac{l_{3y}}{l_{3z}} & 1 \end{bmatrix} \begin{bmatrix} \dot{x} \\ \dot{y} \\ \dot{z} \end{bmatrix}_{\{p\}}$$

(62)

To analyze the contribution of the roll and tilt mechanisms to the induced velocity, Eq.(62) need to be reformulated in terms of the roll and tilt rates $\dot{\psi}$ and $\dot{\theta}_2$. Plugging Eq.(52) into Eq.(44) gives the following expression:

$$\dot{P}_{x\{a\}} = \left(-\sin(\theta_1)L_{ID} + \sin(\theta_2 - \phi_3)L_{DP}\right)\dot{\theta}_2$$
$$\dot{P}_{y\{a\}} = \left(\cos(\theta_1)L_{ID} - \cos(\theta_2 - \phi_3)L_{DP}\right)\dot{\theta}_2$$

(63)

Let:

$$C = -\sin(\theta_1)L_{ID} + \sin(\theta_2 - \phi_3)L_{DP}$$
$$D = \cos(\theta_1)L_{ID} - \cos(\theta_2 - \phi_3)L_{DP}$$

(64)

Then

$$\dot{P}_{x\{a\}} = C\dot{\theta}_2$$
$$\dot{P}_{z\{a\}} = D\dot{\theta}_2$$

(65)

Substituting Eq.(65) into Eq.(61), Eq.(62) becomes:

$$
\begin{bmatrix} \dot{q}_1 \\ \dot{q}_2 \\ \dot{q}_3 \end{bmatrix} = \begin{bmatrix} \frac{l_{1x}}{l_{1z}} & \frac{l_{1y}}{l_{1z}} & 1 \\ \frac{l_{2x}}{l_{2z}} & \frac{l_{2y}}{l_{2z}} & 1 \\ \frac{l_{3x}}{l_{3z}} & \frac{l_{3y}}{l_{3z}} & 1 \end{bmatrix} \begin{bmatrix} C\dot{\theta}_2 \\ -\sin(\psi)D\dot{\theta}_2 - \cos(\psi)(P_{z\{a\}} + d_3)\dot{\psi} \\ \cos(\psi)D\dot{\theta}_2 - \sin(\psi)(P_{z\{a\}} + d_3)\dot{\psi} \end{bmatrix}
$$

$$
= \underbrace{\begin{bmatrix} \frac{l_{1x}}{l_{1z}} & \frac{l_{1y}}{l_{1z}} & 1 \\ \frac{l_{2x}}{l_{2z}} & \frac{l_{2y}}{l_{2z}} & 1 \\ \frac{l_{3x}}{l_{3z}} & \frac{l_{3y}}{l_{3z}} & 1 \end{bmatrix} \begin{bmatrix} 0 & C \\ -\cos(\psi)(P_{z\{a\}} + d_3) & -\sin(\psi)D \\ -\sin(\psi)(P_{z\{a\}} + d_3) & \cos(\psi)D \end{bmatrix}}_{\mathbf{M_D}} \begin{bmatrix} \dot{\psi} \\ \dot{\theta}_2 \end{bmatrix}
$$

$$(66)$$

where $\mathbf{M}_D \in \mathbb{R}^{3 \times 2}$ maps $[\dot{\psi}, \dot{\theta}_2]^T$ to $[\dot{q}_1, \dot{q}_2, \dot{q}_3]^T$

From Eq.(55), the tool tip's angular velocities in frame $\{p\}$ are:

$$
\begin{bmatrix} \dot{\theta}_x \\ \dot{\theta}_y \\ \dot{\theta}_z \end{bmatrix}_{\{p\}} = \begin{bmatrix} \dot{\psi} \\ \cos(\psi)\dot{\theta}_2 \\ \sin(\psi)\dot{\theta}_2 \end{bmatrix} \tag{67}
$$

Since there's no rotational transformation between base frame $\{b\}$ and delta platform frame $\{p\}$, $[\dot{\theta}_x, \dot{\theta}_y, \dot{\theta}_z]^T_{\{p\}} = [\dot{\theta}_x, \dot{\theta}_y, \dot{\theta}_z]^T_{\{b\}}$. From Eq.(67), it's clear that $\dot{\theta}_y$ and $\dot{\theta}_z$ are coupled through ψ and $\dot{\theta}_2$. In other words, specifying $\dot{\theta}_y$ determines a unique corresponding $\dot{\theta}_z$ and vice versa.

Since $\dot{\psi}$ represents the rotational velocity about the base frame's x axis, and the relationship between $\dot{\theta}_y$ and $\dot{\theta}_2$ has been shown in Eq.(67), substituting $\dot{\psi} = \dot{\theta}_x$ and $\dot{\theta}_2 = \frac{1}{\cos(\psi)}\dot{\theta}_y$ into Eq.(66) gives:

$$
\begin{bmatrix} \dot{q}_1 \\ \dot{q}_2 \\ \dot{q}_3 \end{bmatrix} = \mathbf{M_D} \begin{bmatrix} \dot{\theta}_x \\ \frac{1}{\cos(\psi)}\dot{\theta}_y \end{bmatrix}
$$

$$
= \begin{bmatrix} \mathbf{M_D}_{[1,1]} & \frac{1}{\cos(\psi)}\mathbf{M_D}_{[1,2]} \\ \mathbf{M_D}_{[2,1]} & \frac{1}{\cos(\psi)}\mathbf{M_D}_{[2,2]} \\ \mathbf{M_D}_{[3,1]} & \frac{1}{\cos(\psi)}\mathbf{M_D}_{[3,2]} \end{bmatrix} \begin{bmatrix} \dot{\theta}_x \\ \dot{\theta}_y \end{bmatrix} \tag{68}
$$

Let

$$
\mathbf{M_r} = \begin{bmatrix} \mathbf{M_D}_{[1,1]} & \frac{1}{\cos(\psi)}\mathbf{M_D}_{[1,2]} \\ \mathbf{M_D}_{[2,1]} & \frac{1}{\cos(\psi)}\mathbf{M_D}_{[2,2]} \\ \mathbf{M_D}_{[3,1]} & \frac{1}{\cos(\psi)}\mathbf{M_D}_{[3,2]} \end{bmatrix} \tag{69}
$$

Then

$$
\begin{bmatrix} \dot{q}_1 \\ \dot{q}_2 \\ \dot{q}_3 \end{bmatrix}_{induced} = \mathbf{M_r} \begin{bmatrix} \dot{\theta}_x \\ \dot{\theta}_y \end{bmatrix}_{\{b\}} \tag{70}
$$

In this case, it's clear that $\dot{\theta}_z$ has no effect on $\dot{q}_1, \dot{q}_2, \dot{q}_3$. However, to maintain consistency with the full Jacobian inverse expression, $\dot{\theta}_z$ is included on the right-hand side of Eq.(70), yielding:

$$
\begin{bmatrix} \dot{q}_1 \\ \dot{q}_2 \\ \dot{q}_3 \end{bmatrix}_{induced} = [\mathbf{M_r}\ \mathbf{0}] \begin{bmatrix} \dot{\theta}_x \\ \dot{\theta}_y \\ \dot{\theta}_z \end{bmatrix}_{\{b\}} \tag{71}
$$

Note that the joint velocities from Eq.(71) represent the linear velocity induced by roll and tilt. In the Jacobian inverse formulation, Eq.(71) is subtracted from Eq.(60) to eliminate the induced linear velocity.

$$
\begin{bmatrix} \dot{q}_1 \\ \dot{q}_2 \\ \dot{q}_3 \end{bmatrix} = \begin{bmatrix} \dot{q}_1 \\ \dot{q}_2 \\ \dot{q}_3 \end{bmatrix}_{delta} - \begin{bmatrix} \dot{q}_1 \\ \dot{q}_2 \\ \dot{q}_3 \end{bmatrix}_{induced}
$$

$$
= \begin{bmatrix} \frac{l_{1x}}{l_{1z}} & \frac{l_{1y}}{l_{1z}} & 1 \\ \frac{l_{2x}}{l_{2z}} & \frac{l_{2y}}{l_{2z}} & 1 \\ \frac{l_{3x}}{l_{3z}} & \frac{l_{3y}}{l_{3z}} & 1 \end{bmatrix} \begin{bmatrix} \dot{x} \\ \dot{y} \\ \dot{z} \end{bmatrix} - [\mathbf{M_r}\ \mathbf{0}] \begin{bmatrix} \dot{\theta}_x \\ \dot{\theta}_y \\ \dot{\theta}_z \end{bmatrix}
$$

$$
= \begin{bmatrix} \frac{l_{1x}}{l_{1z}} & \frac{l_{1y}}{l_{1z}} & 1 & -\mathbf{M_r}_{[1,1]} & -\mathbf{M_r}_{[1,2]} & 0 \\ \frac{l_{2x}}{l_{2z}} & \frac{l_{2y}}{l_{2z}} & 1 & -\mathbf{M_r}_{[2,1]} & -\mathbf{M_r}_{[2,2]} & 0 \\ \frac{l_{3x}}{l_{3z}} & \frac{l_{3y}}{l_{3z}} & 1 & -\mathbf{M_r}_{[3,1]} & -\mathbf{M_r}_{[3,2]} & 0 \end{bmatrix} \begin{bmatrix} \dot{x} \\ \dot{y} \\ \dot{z} \\ \dot{\theta}_x \\ \dot{\theta}_y \\ \dot{\theta}_z \end{bmatrix}_{\{b\}}
$$

$$(72)$$

Since $\dot{\psi} = \dot{\theta}_x = \dot{q}_4$, $\dot{s} = \dot{q}_5$ and $\dot{\theta}_2 = \frac{1}{\cos(\psi)}\dot{\theta}_y$, the relationship between $\dot{q}_5$ and $\dot{\theta}_y$ can be derived from Eq.(53):

$$
\dot{\theta}_2 = -\frac{L_{DA}L_{JQ}}{L_{ID}L_{AQ}L_{JR}}\dot{s}
$$

$$
\frac{1}{\cos(\psi)}\dot{\theta}_y = -\frac{L_{DA}L_{JQ}}{L_{ID}L_{AQ}L_{JR}}\dot{q}_5 \tag{73}
$$

$$
\dot{q}_5 = -\frac{L_{ID}L_{AQ}L_{JR}}{\cos(q_4)L_{DA}L_{JQ}}\dot{\theta}_y
$$

Thus, all components needed to construct the Jacobian inverse have been derived. By assembling Eq.(73)

with Eq.(72), the joint velocities can be expressed as:

$$
\begin{bmatrix} \dot{q}_1 \\ \dot{q}_2 \\ \dot{q}_3 \\ \dot{q}_4 \\ \dot{q}_5 \end{bmatrix} = \begin{bmatrix} \frac{l_{1x}}{l_{1z}} & \frac{l_{1y}}{l_{1z}} & 1 & -\mathbf{M_r}_{[1,1]} & -\mathbf{M_r}_{[1,2]} & 0 \\ \frac{l_{2x}}{l_{2z}} & \frac{l_{2y}}{l_{2z}} & 1 & -\mathbf{M_r}_{[2,1]} & -\mathbf{M_r}_{[2,2]} & 0 \\ \frac{l_{3x}}{l_{3z}} & \frac{l_{3y}}{l_{3z}} & 1 & -\mathbf{M_r}_{[3,1]} & -\mathbf{M_r}_{[3,2]} & 0 \\ 0 & 0 & 0 & 1 & 0 & 0 \\ 0 & 0 & 0 & 0 & -\frac{L_{ID}L_{AQ}L_{JR}}{\cos(q_4)L_{DA}L_{JQ}} & 0 \end{bmatrix} \begin{bmatrix} \dot{x} \\ \dot{y} \\ \dot{z} \\ \dot{\theta}_x \\ \dot{\theta}_y \\ \dot{\theta}_z \end{bmatrix}
$$
(74)

The analytical expression of the spatial Jacobian inverse of the SHER 3.0 robot is:

$$
\mathbf{J}^{-1} = \begin{bmatrix} \frac{l_{1x}}{l_{1z}} & \frac{l_{1y}}{l_{1z}} & 1 & -\mathbf{M_r}_{[1,1]} & -\mathbf{M_r}_{[1,2]} & 0 \\ \frac{l_{2x}}{l_{2z}} & \frac{l_{2y}}{l_{2z}} & 1 & -\mathbf{M_r}_{[2,1]} & -\mathbf{M_r}_{[2,2]} & 0 \\ \frac{l_{3x}}{l_{3z}} & \frac{l_{3y}}{l_{3z}} & 1 & -\mathbf{M_r}_{[3,1]} & -\mathbf{M_r}_{[3,2]} & 0 \\ 0 & 0 & 0 & 1 & 0 & 0 \\ 0 & 0 & 0 & 0 & -\frac{L_{ID}L_{AQ}L_{JR}}{\cos(q_4)L_{DA}L_{JQ}} & 0 \end{bmatrix}
$$
(75)

2.5 Control Strategy

2.5.1 Model Predictive Control with RCM Constraint

As discussed in the previous section, SHER 3.0 does not have a mechanically enforced RCM. Instead, a virtual RCM constraint is implemented to constrain the robot's motion, and MPC is implemented as the primary control strategy. The system state at time t is defined by the tool tip pose as:

$$
\chi_t = [x, y, z, \theta_x, \theta_y, \theta_z]^T
$$
(76)

and the system input u_t at time t is the joint velocities of the robot:

$$
u_t = [\dot{q}_1, \dot{q}_2, \dot{q}_3, \dot{q}_4, \dot{q}_5]^T
$$
(77)

The cost function is defined as:

$$
C = min \sum_{t=0}^{n-1} \left[(\chi_t - \chi_{\text{des}})Q(\chi_t - \chi_{\text{des}})^T + u_t Ru_t^T + l_t Dl_t^T \right] + \chi_n Q_f \chi_n^T
$$
(78)

s.t.

$$
\chi_{t+1} = \chi_t + \mathbf{J}(q_t)u_t\, dt,
$$
$$
q_{t+1} = q_t + u_t\, dt,
$$
$$
l_t = \|(p_{\text{rcm}} - p) \times \hat{a}_t\|,
$$
$$
\dot{\chi}_{\min} \leq \mathbf{J}(q_t)u_t \leq \dot{\chi}_{\max}
$$
$$
\dot{q}_{\min} \leq u_t \leq \dot{q}_{\max},
$$
$$
Q \succeq 0,\ R \succ 0,\ D \succeq 0,\ Q_f \succeq 0,
$$
.

where target end effector state is represented by χ_{des}, and $\mathbf{J}(q_t) \in \mathbb{R}^{6 \times 5}$ represents the Jacobian matrix of the SHER 3.0 system at joint configuration q_t. The scaler l_t represents the distance between the gripper shaft and the RCM point. And $p_{\text{rcm}} \in \mathbb{R}^3$ is the position vector of the RCM point, p refers to the position vector of the straight shaft tip, and $\hat{a}_t$ indicates the unit vector along the tool shaft direction.

2.5.2 Dual Robot Control Loop

In the SHER 3.0 robot control loop, the input device sent the target tool tip position $x_{des},\ y_{des}\ and\ z_{des}$ to the MPC optimal controller. The desired values are sent to the optimal controller shown in Eq.78, which outputs the joint-velocity command $\dot{q}_{des} \in \mathbb{R}^5$ for SHER 3.0. A motion-limiting block guarantees the safe execution of commanded motions. The limited joint velocity $\dot{q}'_{\text{des}}$ is defined as

$$
\dot{q}'_{\text{des}} = \begin{cases} I^T \dot{q}_{\text{des}}, & \alpha = 1 \\ 0, & \text{otherwise} \end{cases}
$$
(79)

where α is a binary indicator. The mapping function $I \in \mathbb{R}^5$ restricts motion along allowable directions determined by the translational inputs $x_{\text{des}}, y_{\text{des}}, z_{\text{des}}$ from the input device and the current $\dot{\chi}_{\text{real}} \in \mathbb{R}^6$ of the tool pose. The resulting target joint velocity $\dot{q}'_{\text{real}} \in \mathbb{R}^5$ is then sent to the low-level velocity controller, which moves the five joints of SHER 3.0. The joint velocity $\dot{q}_{\text{real}}$ is used to update the Jacobian $\mathbf{J}$ in Eq. 57 for the next iteration and compute the corresponding Cartesian tip velocity $\dot{\chi}_{\text{real}}$.

Designed specifically for SHER 3.0, the I²RIS micromanipulator extends the system with two extra degrees of freedom [21]; however, in our experiment, it is operated as a straight surgical tool. I²RIS control loop used single PD control. The input device sent desired orientation $\theta_{x_{des}}$, $\theta_{y_{des}}$, and $\theta_{z_{des}}$ to the micro manipulator's
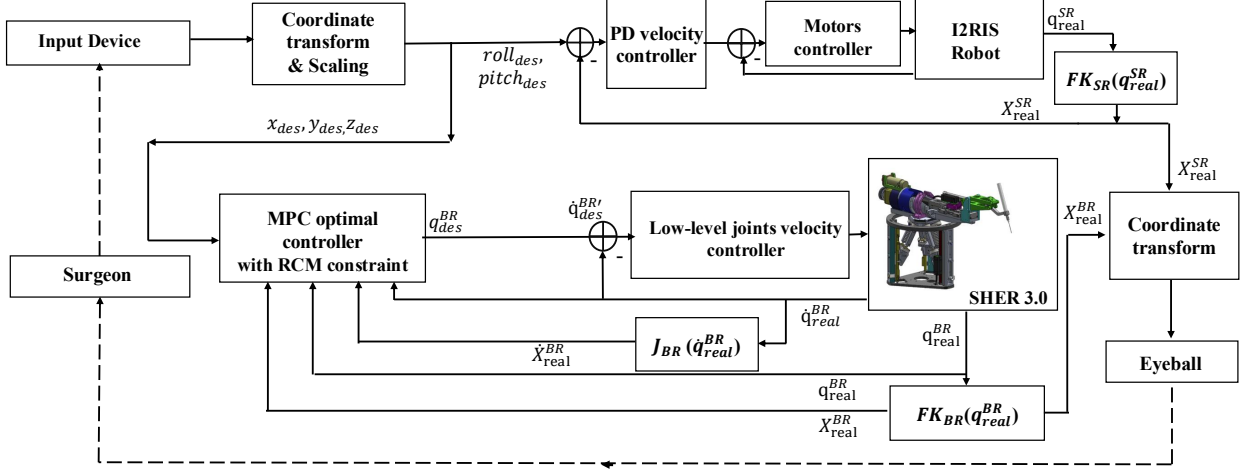
Fig. 6: Control loop diagram of the MPC-based teleoperation control for SHER 3.0

motors. The target input drives the I²RIS to move in different directions.

Fig.6 shows the detailed control loop diagram for this MPC-based teleoperation controller. To avoid confusion, note that the notations used in the figure differ slightly from those in the main text: BR denotes the Base Robot (SHER 3.0), and SR denotes the micro manipulator (I²RIS).

3 EXPERIMENTS

To evaluate the overall performance of the proposed kinematics and Jacobian models and the MPC-based RCM control algorithm, two distinct experiments were conducted, each targeting a specific goal as follows:

1. *Kinematics Analysis*: To analyze the kinematic performance of SHER 3.0.
2. *RCM Control Evaluation*: To evaluate the performance of the implementation of the MPC control algorithm and analyze the accuracy of the robot kinematics and Jacobian in maintaining the RCM constraint.

3.1 Experimental Setup

Fig. 7 illustrates the experimental setup, which includes the SHER 3.0 with a motion controller (Galil, CA, USA) for low-level joint velocity control. A 6-DoF force/torque sensor (Nano17, ATI Industrial Automation, NC, USA) is attached to SHER's end-effector to measure the forces/torques applied by the user's hand and to enable cooperative control in an admittance-based strat-

egy [13]. The high-level MPC controller with RCM constraint, mid-level inverse kinematics solver, and low-level joint velocity controller were all implemented in C++ using the CISST-SAW libraries, running at an update rate of 200 Hz [22]. To evaluate the RCM control accuracy, a set of 3-millimeter ArUco markers were rigidly mounted on the robot's end-effector, tracking its position and orientation using a digital microscope (AD407, Andonstar, China) calibrated using a standard pinhole camera model. A 3D-printed eye phantom with a diameter of 24 mm (typical human eye diameter), incorporates a gimbal joint that functions as the RCM to simulate the sclerotomy. The robotic instrument shaft is inserted through the gimbal joint, simulating the RCM constraint during the eye surgery procedures.

3.2 Experimental Procedures
3.2.1 Kinematics Analysis

The SHER 3.0 kinematic relations are modeled in Python and analyzed based on several kinematics-related metrics, such as reachable and dexterous workspaces, and manipulability index. The reachable and dexterous workspaces are evaluated and presented for the entire SHER 3.0 robot end-effector (Delta stage combined with the roll-tilt mechanism). The manipulability index are evaluated and presented for the parallel Delta stage and the roll-tilt mechanism separately.

In this work, the dexterous workspace of SHER 3.0 is defined as the subset of the reachable workspace that has more than one inverse kinematic solution. This concept aligns with prior microsurgical robot research [23].

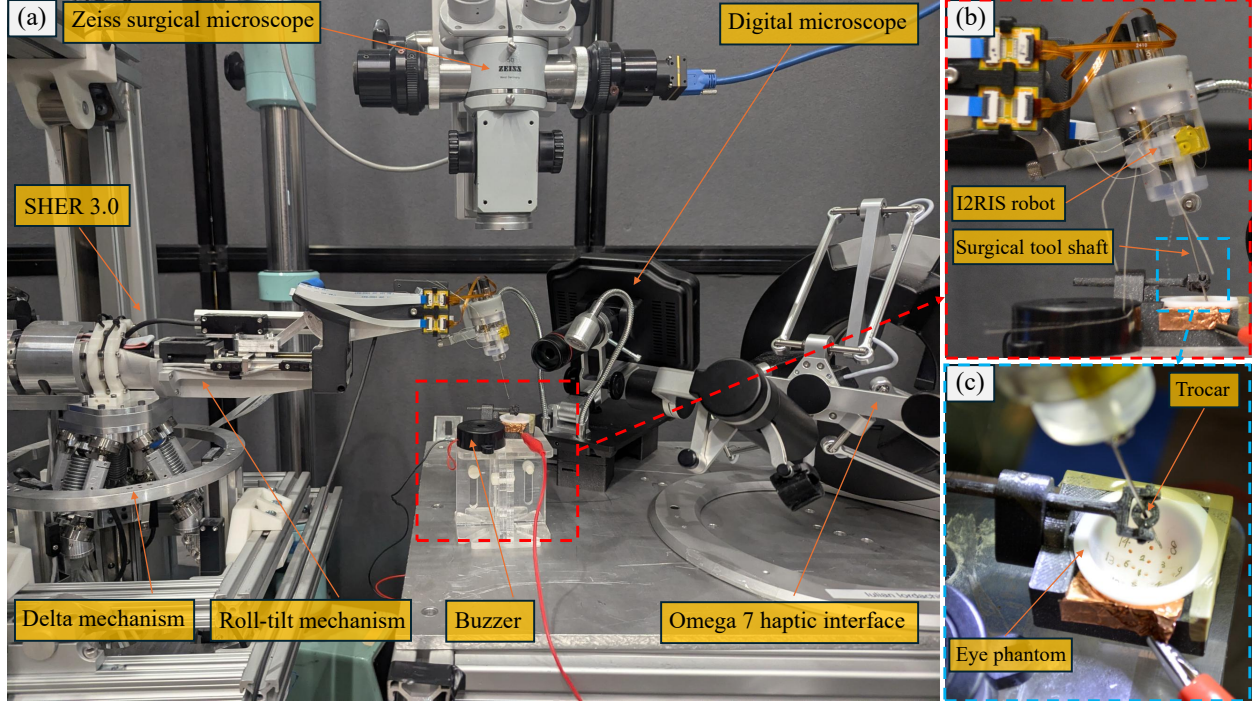The manipulability of the roll–tilt mechanism and

Fig. 7: Experimental setup includes SHER 3.0, an Omega 7 haptic interface, a surgical microscope, and a digital microscope to track the robot end-effector motion (left). A surgical instrument (the I²RIS robot) is attached to the SHER 3.0 (top right), and its shaft passes through a trocar (simulating RCM) to enter the eye phantom (bottom right).
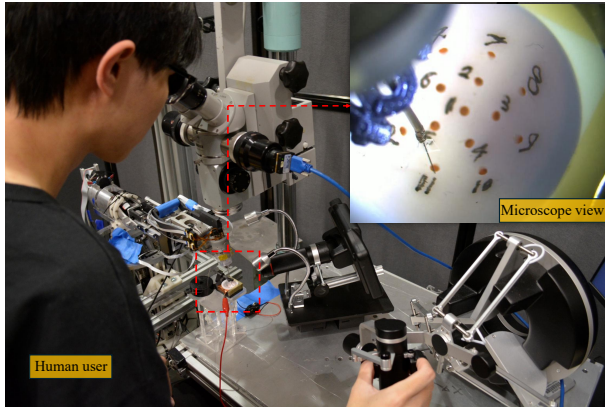

Fig. 8: Experimental procedure.

the delta platform of SHER 3.0 are evaluated using Yoshikawa's classical manipulability index [24], which quantifies the isotropy of velocity transmission between joint space and task space. The manipulability index is defined as:

$$w = \sqrt{\det(\mathbf{J}^T \mathbf{J})} \qquad (80)$$

where $\mathbf{J}$ is the Jacobian matrix of the robot, and w represents the volume of the velocity manipulability ellipsoid, which indicates the ability of the end-effector to generate arbitrary motion directions given bounded joint inputs. A smaller w corresponds to configurations where the mechanism loses directional controllability.

To facilitate interpretation of the manipulability distribution of the roll–tilt and the delta mechanism, a normalized manipulability index is introduced here:

$$w_{norm} = \frac{w}{w_{max}} \qquad (81)$$

where w_{max} is the maximum manipulability index within the considered joint and task space.

3.2.2   RCM Control Evaluation

To assess the performance of the robot kinematics and the MPC control algorithm in maintaining the RCM constraint safely and accurately, we conducted a pilot study experiment with five users in a teleportation framework (see Fig. 8).

Before the experiments began, the participants were asked to manipulate the robot in free space using a hap-

tic interface to familiarize themselves with the setup and adjust the seat and robot position and microscope focus based on their preference.

The experiment includes inserting a surgical instrument through the trocar into the eye phantom, manipulating the instrument towards a set of target points (five points selected in a random order), and touching the points with the tool tip (this is considered as one trial). An electrical buzzer is used to confirm the touch (see the bottom row of Fig. 9). Each participant completed five trials, and the sequence of the target points was identical across all users for consistency. The robot end-effector motion was tracked using two external microscopes and ArUco markers for later analysis of RCM constraint accuracy. Of note, at the tip of the surgical instrument, the wrist-like snake robot, I^{2}RIS, can be bent in two directions to enable an optimum approach angle (for example, perpendicular) to the retinal surface; however, it is operated as a straight surgical tool in this experiment – the kinematic modeling and control of that micro robot is beyond the scope of this work (see the top row of Fig. 9).

4   RESULTS

This section presents the results using two main approaches: a theoretical approach that performs a kinematics analysis of the SHER 3.0 robot, studying the kinematics performance of the robot mechanism design, followed by an experimental approach that validates the accuracy and performance of the RCM control implementation within a pilot study teleportation experiment with five users.

4.1   Kinematics Analysis

4.1.1   Workspace Analysis

The reachable and dexterous workspaces of SHER 3.0 are shown in Fig. 10, which includes the 3D workspaces (Fig. 10-a) and their corresponding 2D projections on the XY, XZ, and YZ planes (Figs. 10-b to 10-d). The volumes of the reachable and dexterous workspaces are calculated as 8.878×10^5 mm^3 and 1.977×10^5 mm^3, respectively, with a dexterous-to-reachable ratio of 22.27% as shown in Table 1.

4.1.2   Manipulability Analysis

For the delta platform, the normalized manipulability volume in joint space is plotted as functions of the three joint variables q_1, q_2, q_3, and in task space as a function of the Cartesian coordinates x, y, z, as shown in Fig. 11. As shown in Fig. 11-a and 11-b, the delta mechanism has

Table 1: Kinematic performance metrics of SHER 3.0. (Delta) and (RT) denote the Delta platform and the roll–tilt mechanism.

Metric	Value
Reachable workspace vol. (mm^3)	8.878×10^5
Dexterous workspace vol. (mm^3)	1.977×10^5
Dexterous-to-reachable ratio	22.27%
Max manipulability (Delta)	1.0
Min manipulability (Delta)	4.4×10^{-5}
Mean manipulability (Delta)	0.426
Std. of manipulability (Delta)	0.275
Max manipulability (RT)	1.0
Min manipulability (RT)	0.046
Mean manipulability (RT)	0.286
Std. of manipulability (RT)	0.205

higher manipulability when the three joint values are similar. Correspondingly, Fig. 11-c and 11-d indicate that the region of highest manipulability forms an approximately cylindrical core near the center of the delta's reachable task space. The maximum, minimum, and mean values of the normalized manipulability index for the delta mechanism are 1.0, 4.4×10^{-5} and 0.426 respectively, with a standard deviation of 0.275 as shown in Table 1.

For the roll–tilt mechanism, the normalized manipulability surface is plotted as a function of the two joint variables $q_4 = \psi$ and $q_5 = s$, as shown in Fig. 12. It is observed that the roll-tilt mechanism has its minimum normalized manipulability index around the two near-singular configurations at joint variable $s \approx 25$ mm and $s \approx 50$ mm, with corresponding tool angles $\theta_{tool} = 133.7°$ and $\theta_{tool} = 159.1°$ (see Figs. 12-b and 12-c). The maximum, minimum, and mean values of the normalized manipulability index for the roll-tilt mechanism are 1.0, 0.046 and 0.286, respectively, with a standard deviation of 0.205 as shown in Table 1.

4.2   RCM Control Tests

Five male users, with ages ranging from 24 to 40 (mean 29.8), participated in this pilot study teleportation experiment. We employed the 10-item Edinburgh Handedness Inventory (EHI) score to evaluate the handedness of the users [25]. All users were dominantly right-handed with a Laterality Quotient (LQ) of 100.00 ± 0.00. A to-
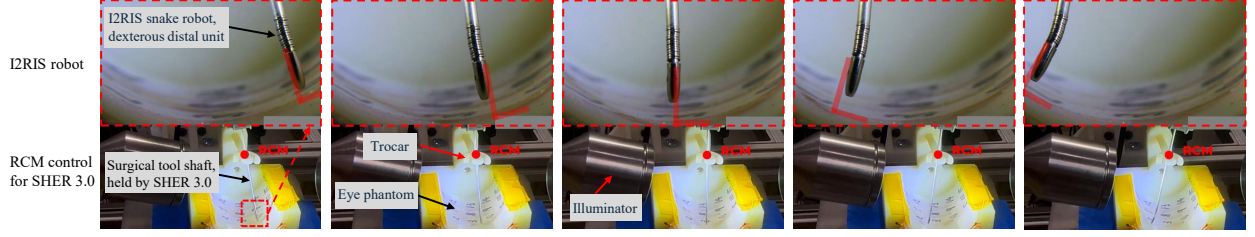
Fig. 9: RCM constraint implementation on SHER 3.0: The shaft of the surgical instrument attached to the SHER 3.0 end-effector pivots through a trocar point (bottom row). The I²RIS snake robot, attached to the distal end of the surgical instrument, enables an optimum approach angle (perpendicular in this case) to the retinal surface (top row).
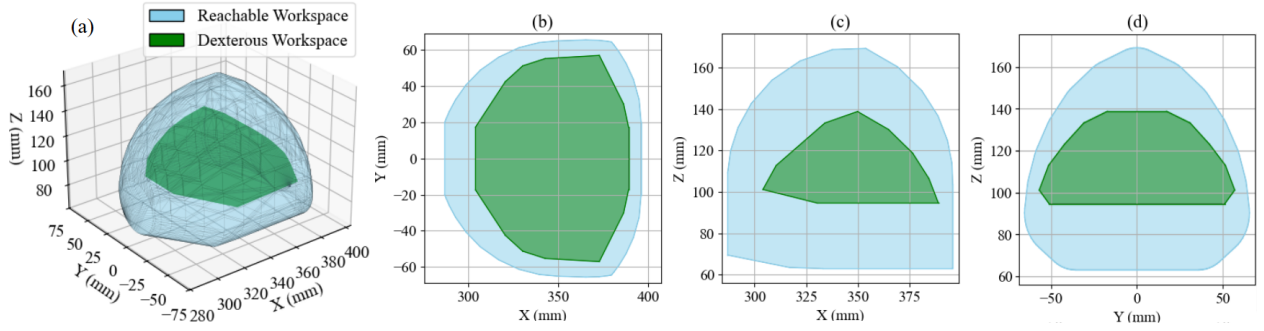

Fig. 10: Reachable and dexterous workspaces of SHER 3.0: (a) 3D view and (b) XY, (c) XZ, (d) YZ planar views.
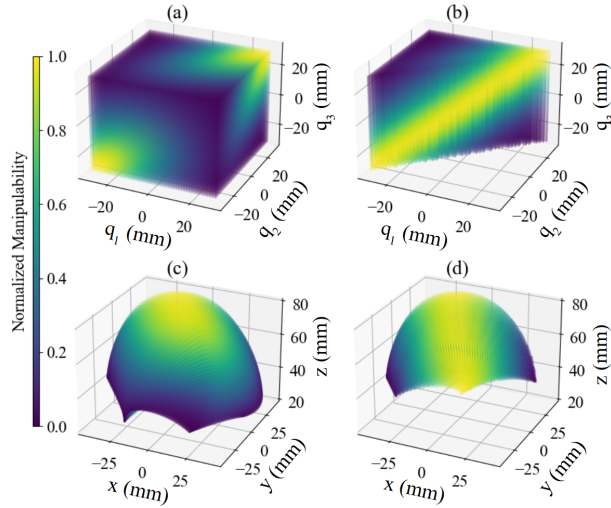

Fig. 11: Normalized manipulability index of the delta platform: (a) distribution in joint space and (c) in task space. Plots (b) and (d) show corresponding 45° cross-sectional views of the joint space and task space, respectively.

the trajectory (position and orientation) of the shaft of a surgical tool (attached to SHER 3.0 end-effector), which passed through the trocar point on the eye phantom during the teleportation experiments. The blue curve shows the tip trajectory of the surgical tool while touching the target points. The dashed lines represent the footprint of the position/orientation of the tool shaft during a single trial. The RCM error, defind as the distance between the closests point on the tool shaft to the trocar hole, is measured as 0.55 ± 0.12 mm with a maximum error value of 0.73 mm, which satisfies the clinical requirements for doing a safe robot-assisted manipulation of surgical instruments inside the eye. Of note, the inner diameter of a typical trocar used in retinal surgery is 0.89 mm (20-gauge) [26].

Table 2: Results for the RCM control experiment

Metric	Value
Max. RCM error (mm)	0.73
Min. RCM error (mm)	0.01
Mean RCM error (mm)	0.55
Std. of RCM error (mm)	0.12

tal of 25 trials are collected from the users, and the results of the accuracy of the RCM control algorithm are summarized in Table 2. Fig. 13 illustrates an example of
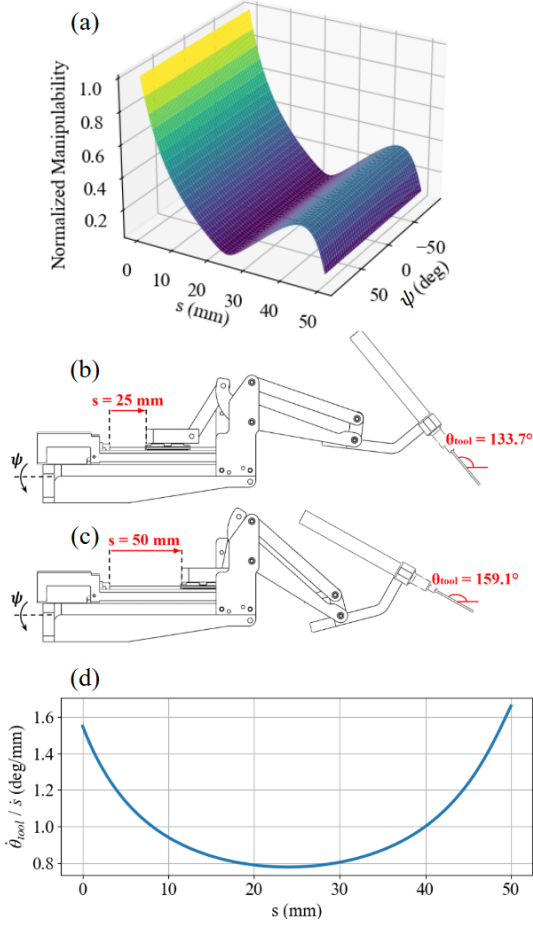
Fig. 12: Normalized manipulability index of the roll–tilt mechanism: (a) overall distribution across the joint space; (b) near-singular configuration at $s = 25$ mm, with corresponding $\theta_{tool} = 133.7°$; (c) near-singular configuration at $s = 50$ mm, with corresponding $\theta_{tool} = 159.1°$. (d) Tool-to-stroke velocity ratio with stroke length ranging from 0 to 50 mm.
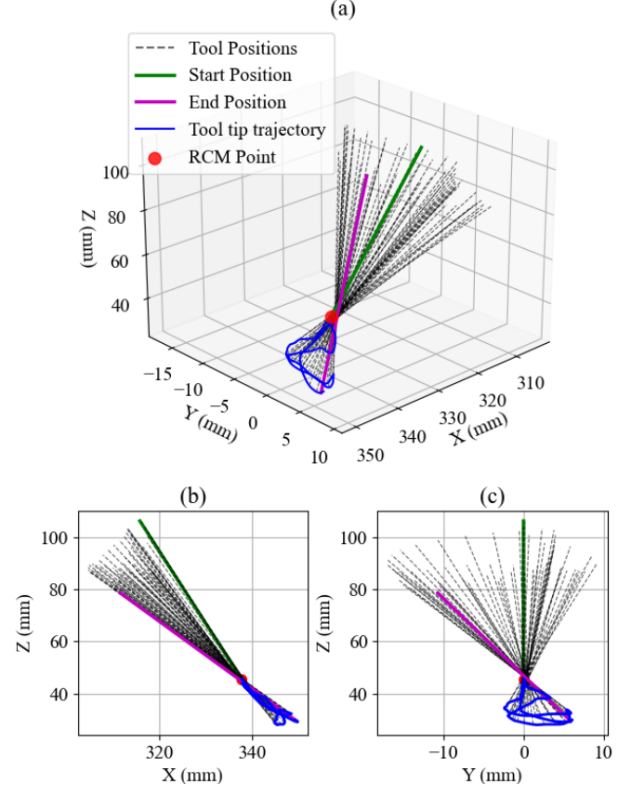

Fig. 13: Visualization of one trial from the RCM experiments: (a) tool tip path with the start and end tool positions highlighted, and (b) XZ plane, (c) YZ plane projections.

5 DISCUSSION AND FUTURE WORK

The forward and inverse kinematics (Eq.27, Eqs.30-33) along with the Jacobian and Jacobian inverse (Eq.57, Eq.75) for the SHER 3.0 robotic system are derived in closed form, which significantly reduces computational load compared to numerical methods and thus facilitates real-time implementation. The workspace analysis demonstrates that the dexterous workspace of SHER 3.0 is sufficient to cover the target operational region, corresponding to the patient's eyeball with an approximate diameter of 24 mm. This confirms that the robot can achieve full dexterity within the surgical workspace, enabling flexible tool positioning and orientation during

microsurgical procedures. The manipulability analysis shows two notable singularities: at s ≈ 25 mm, where the tool-tip velocity is significantly reduced, which is consistent with the discovery in the prior work [20] for this type of tilt mechanism; while at s ≈ 50 mm, the mechanism approaches its designed limits. These findings highlight the regions in which the robot operates with reduced manipulability and can inform safe operational boundaries during surgical tasks.

One limitation of this work is the number of users (five). This is a pilot study that focuses on the validation of the proposed kinematics models and the feasibility of the SHER 3.0 robotic system and the MPC control algorithm in an RCM constraint satisfaction in an artificial eye phantom. Another limitation has to do with the eye phantom. The phantom used in this experiment is a 3D-printed component that simulates the RCM constraint at the eye sclerotomy. Still, it has a relatively rigid trocar without sufficient deformability similar to that of human sclera tissue.

To address these limitations in our future works and to improve experimental realism, we plan to expand the study to multiple users and adopt high-fidelity synthetic eye models—specifically Bioniko phantoms—which are designed to mimic the structural and mechanical properties of human eyes.

6 CONCLUSION

This work presents, for the first time, a thorough analytical forward and inverse kinematics and Jacobian models for the SHER 3.0, with a Delta-based parallel-serial mechanism. Based on these analytical models, a MPC algorithm is designed to maintain a RCM constraint at eye sclerotomy during robot-assisted retinal microsurgical procedures. A kinematics analysis is performed to calculate the reachable and dexterous workspaces of the robot. Moreover, the manipulability performance of the SHER 3.0 is evaluated across the robot's joint space and end-effector task space. Finally, the accuracy of the MPC-based controller in enforcing the RCM constraint is evaluated in a pilot study of a teleportation experiment. Experimental results demonstrate that the proposed kinematics and Jacobian models, together with the MPC control algorithm, satisfy clinical requirements for RCM accuracy, providing a safe and precise robot-assisted retinal surgery platform with robust control performance.

CONFLICT OF INTEREST

The authors declare no conflicts of interest.

DATA AVAILABILITY STATEMENT

The authors attest that all data related to this study are included in the paper.

REFERENCES

[1] Taghirad, H. D., 2025, *Parallel robots: mechanics and control* CRC press.

[2] Müller, A., 2025, "Parallel robots," *Robotics Goes MOOC: Design*, pp. 89–165.

[3] Han, G., Xie, F., Liu, X.-J., Meng, Q., and Zhang, S., 2020, "Technology-oriented synchronous optimal design of a 4-degrees-of-freedom high-speed parallel robot," *Journal of Mechanical Design,* **142**(10), p. 103302.

[4] Huang, T., Li, Z., Li, M., Chetwynd, D. G., and Gosselin, C. M., 2004, "Conceptual design and dimensional synthesis of a novel 2-dof translational parallel robot for pick-and-place operations," *J. Mech. Des.,* **126**(3), pp. 449–455.

[5] Han, Y., and Guo, W., 2022, "A computable framework to efficiently design both current and robotic legged landers for extraterrestrial exploration mission," *Journal of Mechanical Design,* **144**(1), p. 014501.

[6] Coppola, G., Zhang, D., Liu, K., and Gao, Z., 2013, "Design of parallel mechanisms for flexible manufacturing with reconfigurable dynamics," *Journal of mechanical design,* **135**(7), p. 071011.

[7] Russo, M., Zhang, D., Liu, X.-J., and Xie, Z., 2024, "A review of parallel kinematic machine tools: Design, modeling, and applications," *International Journal of Machine Tools and Manufacture,* **196**, p. 104118.

[8] Khalifa, A., Fanni, M., Mohamed, A. M., and Miyashita, T., 2018, "Development of a new 3-dof parallel manipulator for minimally invasive surgery," *The International Journal of Medical Robotics and Computer Assisted Surgery,* **14**(3), p. e1901.

[9] Aginaga, J., Iriarte, X., Plaza, A., and Mata, V., 2018, "Kinematic design of a new four degree-of-freedom parallel robot for knee rehabilitation," *Journal of Mechanical Design,* **140**(9), p. 092304.

[10] Nakano, T., Sugita, N., Ueta, T., Tamaki, Y., and Mitsuishi, M., 2009, "A parallel robot to assist vitreoretinal surgery," *International journal of computer assisted radiology and surgery,* **4**(6), pp. 517–526.

[11] Nasseri, M. A., Eder, M., Nair, S., Dean, E., Maier, M., Zapp, D., Lohmann, C. P., and Knoll, A., 2013, "The introduction of a new robot for assistance in ophthalmic surgery," In 2013 35th Annual International Conference of the IEEE Engineering in Medicine and Biology Society (EMBC), IEEE, pp. 5682–5685.

[12] Vander Poorten, E., Riviere, C. N., Abbott, J. J., Bergeles, C., Nasseri, M. A., Kang, J. U., Sznitman, R., Faridpooya, K., and Iordachita, I., 2020, "Robotic retinal surgery," In *Handbook of robotic and image-guided surgery*. Elsevier, pp. 627–672.

[13] Üneri, A., Balicki, M. A., Handa, J., Gehlbach, P., Taylor, R. H., and Iordachita, I., 2010, "New steady-

hand eye robot with micro-force sensing for vitreoretinal surgery," In 2010 3rd IEEE RAS & EMBS International Conference on Biomedical Robotics and Biomechatronics, IEEE, pp. 814–819.

[14] Zhao, B., Esfandiari, M., Usevitch, D. E., Gehlbach, P., and Iordachita, I., 2023, "Human-robot interaction in retinal surgery: A comparative study of serial and parallel cooperative robots," In 2023 32nd IEEE International Conference on Robot and Human Interactive Communication (RO-MAN), IEEE, pp. 2359–2365.

[15] Dehghani, S., Sommersperger, M., Zhang, P., Martin-Gomez, A., Busam, B., Gehlbach, P., Navab, N., Nasseri, M. A., and Iordachita, I., 2023, "Robotic navigation autonomy for subretinal injection via intelligent real-time virtual ioct volume slicing," In IEEE International Conference on Robotics and Automation: ICRA:[proceedings]. IEEE International Conference on Robotics and Automation, Vol. 2023, p. 4724.

[16] Alamdar, A., Usevitch, D. E., Wu, J., Taylor, R. H., Gehlbach, P., and Iordachita, I., 2023, "Steady-hand eye robot 3.0: Optimization and benchtop evaluation for subretinal injection," *IEEE transactions on medical robotics and bionics,* **6**(1), pp. 135–145.

[17] Karmakar, S., and Turner, C. J., 2024, "A literature review on stewart–gough platform calibrations," *Journal of Mechanical Design,* **146**(8), p. 083302.

[18] Xiao, B., Alamdar, A., Song, K., Ebrahimi, A., Gehlbach, P., Taylor, R. H., and Iordachita, I., 2022, "Delta robot kinematic calibration for precise robot-assisted retinal surgery," In 2022 International Symposium on Medical Robotics (ISMR), IEEE, pp. 1–7.

[19] Li, Y., and Xu, Q., 2005, "Kinematic analysis and dynamic control of a 3-puu parallel manipulator for cardiopulmonary resuscitation," In ICAR'05. Proceedings., 12th International Conference on Advanced Robotics, 2005., IEEE, pp. 344–351.

[20] Roth, R., Wu, J., Alamdar, A., Taylor, R. H., Gehlbach, P., and Iordachita, I., 2021, "Towards a clinically optimized tilt mechanism for bilateral micromanipulation with steady-hand eye robot," In 2021 International Symposium on Medical Robotics (ISMR), IEEE, pp. 1–7.

[21] Jinno, M., and Iordachita, I., 2021, "Improved integrated robotic intraocular snake: Analyses of the kinematics and drive mechanism of the dexterous distal unit," *Journal of medical robotics research,* **6**(01n02), p. 2140001.

[22] Deguet, A., Kumar, R., Taylor, R., and Kazanzides, P., 2008, "The cisst libraries for computer assisted intervention systems," In MICCAI Workshop on Systems and Arch. for Computer Assisted Interventions, Midas Journal, Vol. 71.

[23] Hoshyarmanesh, H., Zareinia, K., Lama, S., and Sutherland, G. R., 2021, "Structural design of a microsurgery-specific haptic device: neuroarm-plushd prototype," *Mechatronics,* **73**, p. 102481.

[24] Yoshikawa, T., 1985, "Manipulability of robotic mechanisms," *The international journal of Robotics Research,* **4**(2), pp. 3–9.

[25] Oldfield, R. C., 1971, "The assessment and analysis of handedness: the edinburgh inventory," *Neuropsychologia,* **9**(1), pp. 97–113.

[26] Mohamed, S., Claes, C., and Tsang, C. W., 2017, "Review of small gauge vitrectomy: progress and innovations," *Journal of ophthalmology,* **2017**(1), p. 6285869.